Aerospace Science and Technology 122 (2022) 107408

Contents lists available at ScienceDirect

Aerospace Science and Technology

www.elsevier.com/locate/aescte

Three-dimensional flow structures and heat transfer characteristics of compressible flow over a cylindrical cavity

Jiangtao Wang [a,b], Te Ma [b], Zhe Wang [b], Ruixing Wang [b,*], Hongwei Song [b], Wu Yuan [b], Hongwei Zheng [c]

[a] Wide Range Flight Engineering Science and Application Center, Institute of Mechanics, Chinese Academy of Sciences, Beijing 100190, China
[b] Key Laboratory for Mechanics in Fluid-Solid Coupling Systems, Institute of Mechanics, Chinese Academy of Sciences, Beijing 100190, China
[c] State Key Laboratory of High-Temperature Gas Dynamics, Institute of Mechanics, Chinese Academy of Sciences, Beijing 100190, China

ARTICLE INFO

Article history:
Received 1 April 2021
Received in revised form 20 October 2021
Accepted 8 February 2022
Available online 11 February 2022
Communicated by Yu Lv

Keywords:
Cylindrical cavity
Heat transfer
Compressible flow
3D flow behaviors

ABSTRACT

High-speed flows over a cavity produce remarkably local heat augments. Heat transfer characteristics of compressible flow over a cylindrical cavity were revealed using wind tunnel experiments and computational analysis. Heating augmentation induced by cylindrical cavities is significant near the trailing edge of the cavity and distributed in a finite width along the spanwise direction. The heating augmentation of the cylindrical cavity decreases with the decrease in the ratio of cavity diameter (D) to cavity depth (H). Relationships between heat transfer and flow structures of the cylindrical cavity are observed. 3D geometric features of the cylindrical cavity lead to the formation of slant recirculating eddy and the existence of symmetric open flow regions in both spanwise sides of the closed cavity.

© 2022 Elsevier Masson SAS. All rights reserved.

1. Introduction

Studies on cavity flows are highly interesting in engineering applications, such as weapon bays and landing gears of aircraft, sunroofs of automotive, and mixing control for supersonic combustion [1–6]. A large body of previous studies mainly focuses on the complex flow mechanisms, acoustic instabilities, wave interactions, and the corresponding flow control techniques. Based on its flow characteristics, cavities are also commonly used as the flame holder in the ramjet [7–12]. The unique flow characteristics of the cavity also cause the change of the heat transfer characteristics of the cavity and its surrounding area. A typical case is the accident of the space shuttle Columbia in February 2003 [13]. The rectangular cavity, as the local damage in the heat shield, causes heating augmentation in supersonic/hypersonic flows and brings disastrous effects [14,15]. The geometry of cavities in reality is not limited to rectangular. The existence of particle collision, screw sealing holes may form the cylindrical cavities. Therefore, understanding heat transfer induced by a cylindrical cavity in a high-speed flow has important theoretical and practical significance.

In general, a 2D cavity can be divided into two stable flow regimes based on the length-to-depth (L/H) ratio [16,17]. The cavity with a range of $1 < L/H < 10$ is an open cavity, and the cavity with a range of $L/H > 14$ is a closed cavity. The freestream of the open-cavity flow does not enter the cavity directly and forms an over-cavity shear layer. On the contrary, the mainstream of the closed-cavity flow impinges the cavity floor and forms two backward- and forward-facing step flowfields. The cavity with a range of $10 < L/H < 14$ is a transitional cavity. The flow is unsteady in the case that can form either open- or closed-cavity flows. The characteristics of cavity flow also depend on the external Mach number, the Reynolds number, the ratio of incoming boundary layer thickness to depth, and 3D geometric effects [18–21]. In addition, the upper and lower limits of the transitional cavity do not maintain a fixed value (from 10 to 14). The boundary of cavity flow regimes varies with cavity geometry and Mach numbers [22–24].

Three-dimensional cavities have more complex flow patterns. Regions with strong flow friction often correspond to high heating flux in general. For the rectangular cavity configuration [14,25–27], the numerical and experimental results indicate that strong shear occurs on the cavity's bottom and rear regions, thereby resulting in corresponding local heating augmentation regions. For the cylindrical cavity configuration, only few studies have been carried out and mainly considered incompressible cavity flow patterns [28–30] and strong acoustic effects [31,32]. Hiwada et al. [33] investigated flow and heat transfer characteristics of low-speed cylindrical cavity flow ($U_\infty = 5$–10 m/s). In addition to these typical flow patterns,

* Corresponding author.
E-mail address: wangruixing@imech.ac.cn (R. Wang).

https://doi.org/10.1016/j.ast.2022.107408
1270-9638/© 2022 Elsevier Masson SAS. All rights reserved.

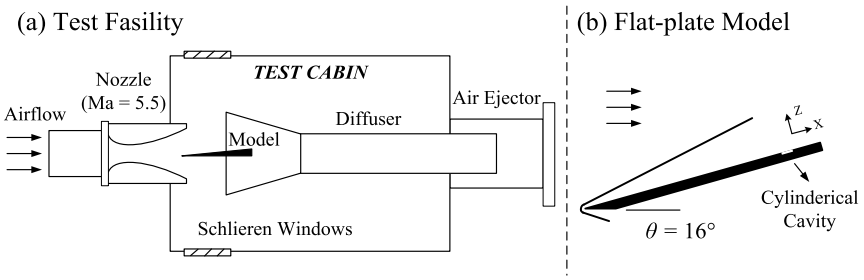

Fig. 1. Sketches of (a) the test cabin of wind tunnel and (b) the flat-plate model with cylinder cavity.

Table 1
Airflow condition in the high-enthalpy free-jet tunnel.

Ma_∞	T_0 (K)	p_0 (MPa)	ρ_∞ (kg/m^3)	T_∞ (K)	Re_∞/m (m^{-1})	θ (°)
5.5	1589.1	3.1	5.06×10^{-2}	229.5	5.66×10^6	16.0

Table 2
Geometries of the cylindrical cavities.

Case	D (mm)	H (mm)	D/H
1	10	1.0	10.0
2		2.0	5.0
3		3.0	3.3
4	20	1.0	20.0
5		2.0	10.0
6		3.0	6.7

an asymmetric flow pattern was noted due to the slant recirculating vortex at $1.4 < D/H < 2.5$ (D is the cavity diameter) in the cylindrical cavity. The curved cylindrical sidewall causes more diverse flow patterns. However, studies on the effects of the cylindrical cavity under compressible flow on heating augmentation are insufficient.

In the present study, experiments have been conducted to determine the heat transfer characteristics of compressible flow over a cylindrical cavity with different diameter-to-depth (D/H) ratios. 3D numerical simulations were also carried out to provide the detailed structure of cylindrical cavity flowfields and heating augmentation mechanisms given that sparsely spaced discrete sensors cannot capture all thermal information.

2. Experimental methods

Experiments were conducted in the high-enthalpy free-jet tunnel (Fig. 1), in the Institute of Mechanics, Chinese Academy of Sciences. Chang et al. provided a detailed description of this wind tunnel facility [34]. The test condition is a free jet with a Mach number of 5.5 (supersonic condition), a total pressure of 3.2 MPa, and a total temperature of 1618.0 K, as shown in Table 1. The length of wind tunnel run time and each test duration are 10.0 s and 4.0 s, respectively. The Schlieren image would be obtained through the optical windows.

The test model consists of a flat plate for a naturally developed turbulent boundary layer and a replaceable plate with a cylindrical cavity. The deflection angle of the flat plate is 16.0°. The center of the cylinder was located 260 mm along the X direction from the leading edge of the flat plate. Geometries of the cylindrical cavities are summarized in Table 2. Three cavities have a diameter D of 10 mm ($D10$ for short), and three other cavities have a diameter of 20 mm ($D20$). The depth H varies from 1.0 mm to 3.0 mm. Thus, the D/H ranges from 3.3 to 20.0. The corresponding unit Reynolds number is approximately 5.66×10^6 per meter. Therefore, the boundary layer at the cavity region is fully turbulent, and the boundary-layer thickness δ is approximately 6 mm with the value of δ/H from 2 to 6.

Heat transfer distribution of the cavity region is measured by coaxial surface thermocouples (type E), with a diameter of 2.0 mm, provided by the State Key Laboratory of High Temperature Gas Dynamics (LHD), Institute of Mechanics, Chinese Academy of Sciences [35]. The thermocouples are set at nine points for the $D20$ cavity (five inside and four outside) and set at five points (one inside and four outside) for the $D10$ cavity; the detailed thermocouple arrangement is shown in Fig. 2. The temperature history is measured by coaxial thermocouple directly, and the heat flux can be derived on the basis of the 1D conduction solutions in a homogeneous semi-infinite solid [36]. The relationship between the heat flux and the measured surface temperature is obtained by the following:

$$q(t) = \frac{1}{\sqrt{\pi}\sqrt{\rho c k}} \int_0^t \frac{dT}{d\tau} \frac{1}{\sqrt{t-\tau}} d\tau \tag{1}$$

where q is the surface heat flux; ρ, c, and k are the density, specific heat, and thermal conductivity of the material, respectively; T is the measured surface temperature; t is time, and τ is the integral variable of time. The value of $\sqrt{\rho c k}$ is 8210 given that the material of the present test models is stainless steel.

3. Experimental results

3.1. Flow survey

The shock angle β on the plate leading edge is visualized using the shadowgraph method. On the basis of the relationship of $\theta - \beta - M$ [37], we obtain the following:

$$\tan\theta = 2\cot\beta \frac{Ma_\infty^2 \sin^2\beta - 1}{Ma_\infty^2(\gamma + \cos 2\beta) + 2} \tag{2}$$

The edge Mach number is approximately 3.8, as shown in Fig. 3. The actual values of the total temperature and total pressure are 1618.0 K and 3.2 MPa, respectively; they differ slightly from the designed values in Table 1.

3.2. Thermocouple results

The wall temperature was measured with ring-distributed thermocouples in Fig. 4. The point where the temperature rises the

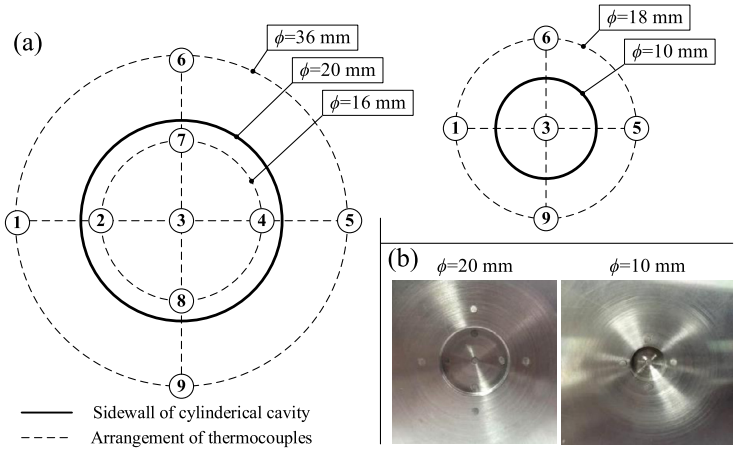

Fig. 2. (a) Schematic of the arrangement of thermocouples in the cavity region, (b) photograph of the thermocouples.

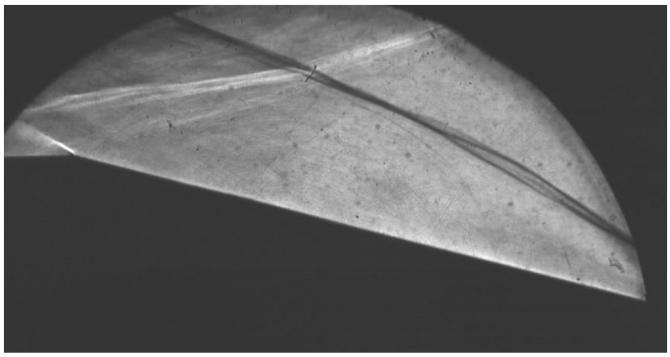

Fig. 3. Spark–Schlieren photograph of a shock wave for the flat plate without the cylindrical cavity.

fastest was near the back edge of the cavity: thermocouple 5 for D10 and thermocouples 4 and 5 for $D20$. The point where the temperature rises the slowest was at the bottom of the cavity: thermocouple 3 for D10 and thermocouple 2 for $D20$. The maximum temperature difference reached almost 135 °C at $t = 4$ s. In addition, some information of spatial heating augmentation distribution at the cavity bottom regions were provided by the comparison of $D20$ cases (Figs. 4(d)–(f)). The effects of heating augmentation for the trailing edge of the bottom increase with the increase in D/H, as shown by the results of thermocouple 4. Slight asymmetry was found in the temperature distribution for thermocouples 7 and 8, most likely due to the instability of the turbulent cavity flow in a spanwise direction. The relations among thermocouples 7 and 8, thermocouple 2, and thermocouple 3 indicated the flow pattern changes from the closed mode to the open mode. A thermal equilibrium state was not achieved during the run as the temperature difference for all the thermocouples continues to increase.

3.3. Distributions of heat flux

Fig. 5 shows the surface heat flux of ring-distributed thermocouples. Apart from thermocouple 2 in $D20$ cases, most surface heat fluxes of the thermocouples declined slightly with the increase in wall temperature. The increase in the surface heat flux of thermocouple 2 indicates in-plane heat conduction at the bottom of the solid cavity zone. The characteristics of heat flux distribution are similar to the change in wall temperature, as shown in Fig. 4.

The result of thermocouple 1 is the reference heat flux q_{ref} for the flat plate flow without cavity affection. The heat flux of other thermocouples is normalized by q_{ref} to assess the effect of heating augmentation in the cavity region. To avoid the effect of the change in wall temperature, data from 0.0 s to 1.0 s in Fig. 5 are adopted to calculate q/q_{ref} and obtain the average as the final results. Normalized surface heat flux at the center of cavity bottom (thermocouple 3) decreases with increasing depth of cavity from 0.71 to 0.36 for $D10$ cases and from 1.32 to 0.64 for $D20$ cases. The peak heat flux appears near the back edge of the cavity (thermocouple 5 for $D10$ and thermocouples 4 for $D20$), within a range of 60–80 kW/m^2. The corresponding normalized peak value varies from 1.57 to 1.30 for $D10$ cases and from 2.04 to 1.42 for $D20$ cases.

Fig. 6 shows the comparison of normalized surface flux q/q_{ref} for $D20$ cases. In the airflow direction, the values of thermocouples 3 to 5 decrease with increasing cavity depth. This finding indicates that the effects of heat augmentation at the back edge reduce with the decrease in D/H. The q/q_{ref} of thermocouple 3 for $D/H = 20$ equals 1.32 (slightly greater than unit), illustrating that the mainstream flow enters the cavity and impinges on the floor. A typical closed cavity regime occurred in this case. The q/q_{ref} of thermocouple 5 for $D/H = 6.67$ equals 1.02 (approximate to 1), illustrating that the mainstream flow does not enter the cavity directly, and the effects of heat augmentation for the open cavity regime is limited. In the spanwise direction, the results of thermocouples 7 and 8 are closed, indicating symmetrical flow patterns. The total aero heating effects on the cavity bottom decrease with decreasing D/H. Comparing with the normalized surface flux results with the D/H of 7.7 in Mach 6 given by reference [14] (the center of the cylinder bottom is approximately 0.5 and the maximum value is approximately 2.0), the orders of magnitude of the present results with the D/H of 6.67 and 10 are similar with them. This also shows the reliability of the data in the present experiments.

3.4. Experimental results summary

A summary of the experimental results is shown in Table 3. The strength of cavity aero heating effects at different locations of cavity region was measured. We noticed that the effects of cavity heating augmentation increase with the increase in D/H. Further study on cavity flowfield structure and its relationships with heating augmentation is discussed in the next section by numerical methods.

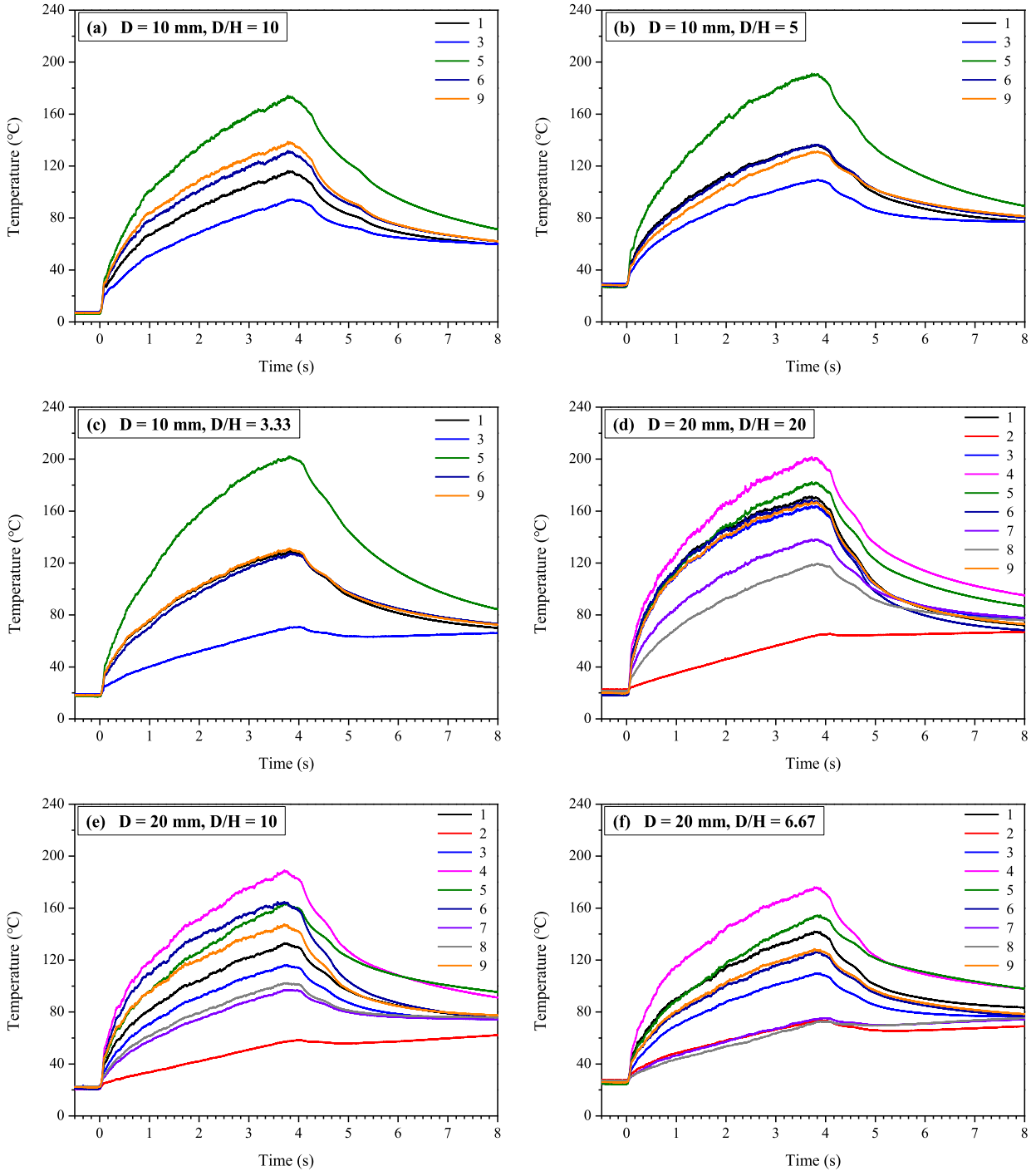

Fig. 4. Thermocouple temperature measurements with wind tunnel running for 4 s: (a)–(c) for cases with $D = 10$ mm, (d)–(f) for cases with $D = 20$ mm. (For interpretation of the colors in the figure(s), the reader is referred to the web version of this article.)

4. Further discussion with computational simulation

The numerical method is applied to analyze the 3D flow and heat transfer characteristics of the cylindrical cavities, which are difficult to observe directly in experiments. The discussion is organized in the following sequence: wall pressure distributions, flow structure, and heat flux distributions of the cylindrical cavity.

4.1. Computation model

The Geometries of the flat plane with a cylinder cavity and the computational domain are presented in Fig. 7(a). The coordinate origin is set at the intersection of the cylinder–cavity central axis and the flat plane surface. The X, Y, and Z coordinates correspond to the downstream direction, the spanwise direction, and the outward normal wall direction, respectively. The flow conditions are based on the experiment setup in Table 1. The boundary conditions include pressure far-field, nonreflection outlet, periodic in the spanwise directions, and no-slip isothermal wall with a constant value of 300 K.

The cavity flow is investigated using a density-based, cell-centered finite volume in-house solver (called *PolyXim*). The solver has shown its robustness and high accuracy on calculating the

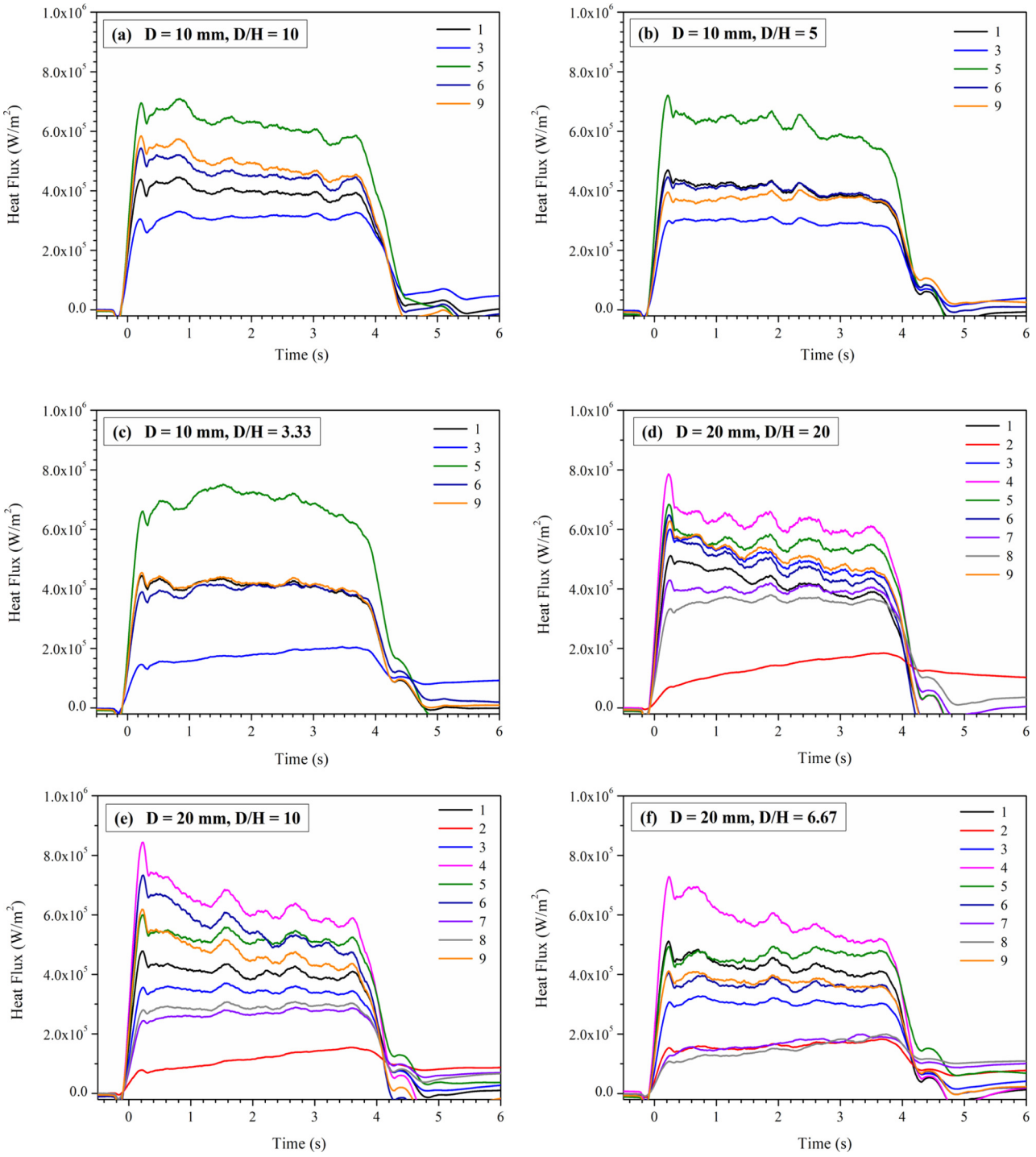

Fig. 5. Surface heat flux results with wind tunnel running for 4 s: (a)–(c) for cases with $D = 10$ mm, (d)–(f) for cases with $D = 20$ mm.

aerodynamic heating flux by several benchmark test cases [38–40]. The numerical results agree well with experimental data. The data parallel implicit method is applied for time discretization, and the MUSCL reconstruction scheme is used for spatial discretization. An improved Green–Gauss method is applied for the calculation of the gradient at the cell centroid. The SST turbulence model is used. Flow unsteadiness of the present simulation was negligible. Instantaneous results are given in the following sections because of the relatively time-invariant imposed flow conditions.

4.2. Validation of computational results

The computational grid is a structured grid with O-block at the cavity region. The first cell height in the normal wall direction is approximately 0.3 μm. The cells in the cavity are nearly isotropic. As shown in Fig. 7(b), the number of grid points inside the cavity for $D20H2$ ($a \times b \times c \times d$) is $101 \times 101 \times 101 \times 121$, and the total number of grid points is approximately 10.6 million. This grid system is the base grid. To investigate the effects of cavity grid density, numerical results with a relatively coarse grid (so-called coarse grid: $a \times b \times c \times d = 51 \times 51 \times 51 \times 81$) and a relatively fine grid (so-called fine grid: $a \times b \times c \times d = 126 \times 126 \times 126 \times 151$)

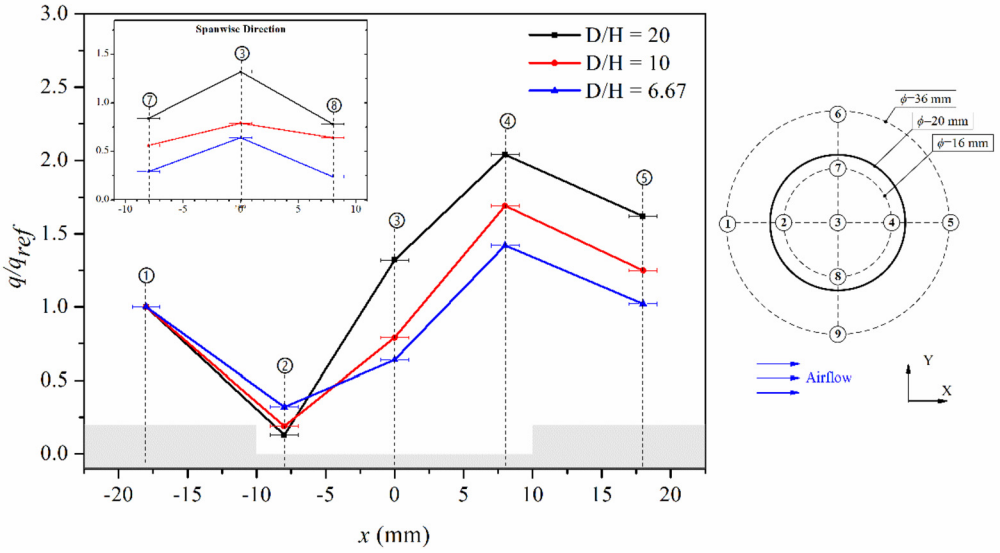

Fig. 6. Comparison of normalized surface flux q/q_{ref} for $D20$ cases with different D/H values. Thermocouples 1 to 5 are assigned along the airflow direction, and thermocouples 7, 3, and 8 are assigned along the spanwise direction.

Table 3
Result summary for maximum temperature $T_{\max}$ (°C) at 4.0 s and average normalized surface heat flux q/q_{ref}, in the first second.

		1	2	3	4	5	6	7	8	9
$D10H1$	$T_{\max}$	116.3	-	94.5	-	174.3	131.8	-	-	138.6
	q/q_{ref}	1	-	0.71	-	1.57	1.20	-	-	1.29
$D10H2$	$T_{\max}$	136.3	-	109.4	-	191.1	136.6	-	-	131.2
	q/q_{ref}	1	-	0.67	-	1.51	0.96	-	-	0.85
$D10H3$	$T_{\max}$	129.3	-	70.8	-	202.2	127.4	-	-	131.5
	q/q_{ref}	1	-	0.36	-	1.30	0.90	-	-	1.02
$D20H1$	$T_{\max}$	171.4	67.5	164.0	201.7	182.2	168.8	138.3	119.4	166.9
	q/q_{ref}	1	0.13	1.32	2.04	1.62	1.21	0.84	0.78	1.21
$D20H2$	$T_{\max}$	133.2	63.2	116.2	189.0	163.6	164.8	97.1	102.4	147.5
	q/q_{ref}	1	0.19	0.79	1.69	1.25	1.51	0.56	0.64	1.26
$D20H3$	$T_{\max}$	142.1	73.7	109.7	176.0	154.4	126.3	75.4	75.9	128.5
	q/q_{ref}	1	0.32	0.64	1.42	1.02	0.81	0.29	0.24	0.83

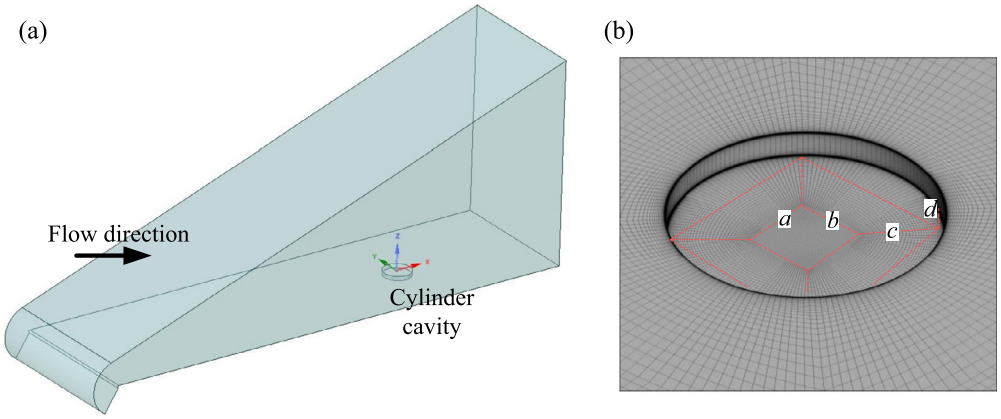

Fig. 7. (a) Geometry of computational domain, and (b) computational base grid of the cylindrical cavity region with O-block.

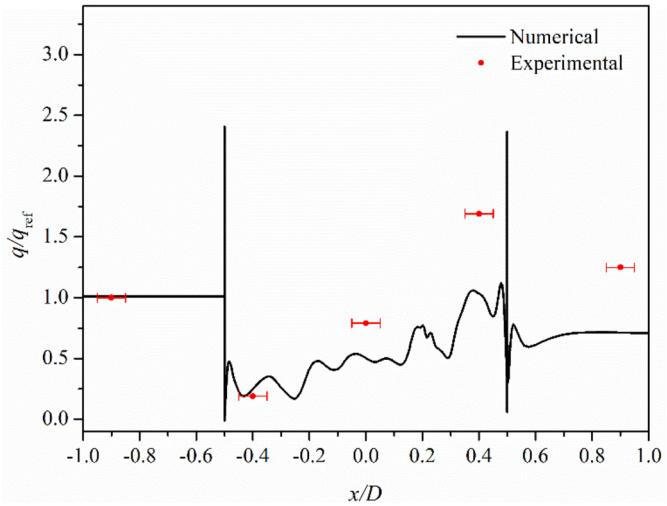

Fig. 8. Comparison of heat flux distribution along the centerline of the cylindrical cavity $D20H2$ between numerical and experimental results.

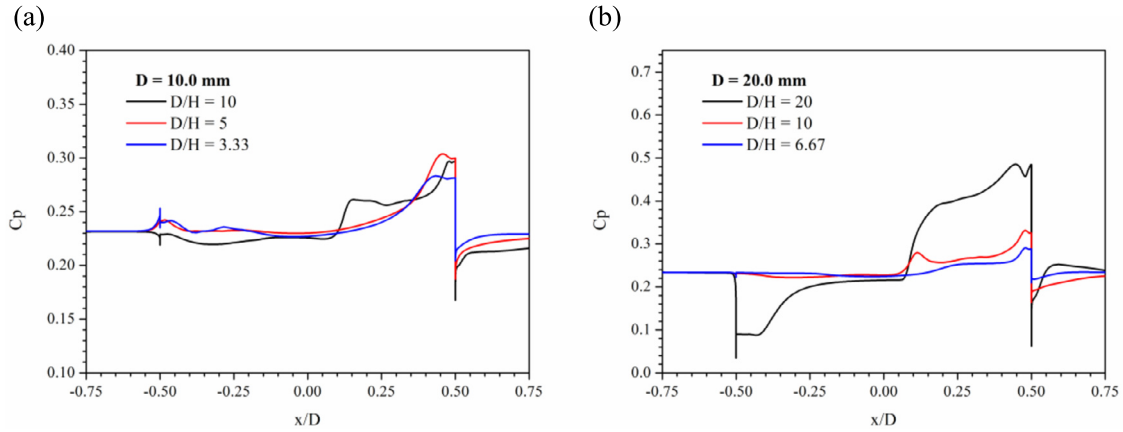

Fig. 9. Pressure coefficient distributions along the centerline of the cylindrical cavity in airflow direction: (a) $D = 10$ mm, (b) $D = 20$ mm.

were compared. In the noncavity region, the grid scales were almost the same. The heat flux distributions of the base grid were almost the same as fine grid, whereas the results of coarse grid underestimated the heat flux of the bottom surface near the trailing edge of the cavity. Therefore, for more reliable discussion and to save computational resource, all computational models are based on the similar grid resolution of base grid.

Numerical and experimental results along the centerline for the $D20H2$ case with base grid are compared in Fig. 8. The numerical heat flux results are slightly less than the thermocouple results. The difference between experimental and numerical results is obtained from the following aspects: (1) the actual measured area of coaxial surface thermocouples with a diameter of 2.0 mm versus ideal geometric assumptions of point and line in the simulation; (2) heat conduction of solid models during the experiments versus constant wall temperature assumption of simulation; (3) the peak of heat flux is not located on the centerline.

4.3. Wall pressure distributions

Fig. 9 shows the wall pressure coefficient along the centerline of the cylindrical cavity in the airflow direction. The wall pressure coefficient is defined as follows:

$$Cp = \frac{2}{\gamma Ma_{\infty}^2}\left(\frac{p}{p_{\infty}} - 1\right). \tag{3}$$

Cylindrical cavity flow regimes with different D/H values are distinguished by referring to the summary of typical cavity floor distributions at subsonic speeds to supersonic speeds in Lawson [3]. The cavity floor distribution of $D/H = 20$ in Fig. 9(b) resembles a typically closed cavity flow. The free-stream flow separates from the front leading edge of the cavity and is attached to the bottom floor. Therefore, adverse pressure distributions develop near the front wall of the cavity, and a region of high pressure develops near the aft wall. The cavity floor distributions of $D/H = 3.33$ and 5 in Fig. 9(a), $D/H = 6.67$ in Fig. 9(b) resemble a typical open cavity flow. The free steam bridges the cavity and impinges the backward-facing step. Therefore, the pressure profile for these cases is relatively flat, and local peaks appear near the aft wall.

Fig. 10 shows the distributions and isopleths of Cp of the bottom of cylindrical cavities with different D/H values. The distributions of Cp are approximately symmetric to the centerline of the cylinder bottom along the airflow direction. The impingement of the shear layer on the aft wall causes a relatively high-value region of Cp near the downstream region in a comparatively wide region. The maximum value of Cp in the case of $D/H = 20$ is higher than the others. This finding suggests a stronger impingement effect with closed cavity flow. For $D/H = 20$, the isoline of Cp is approximately parallel and normal to the free stream, as shown in Fig. 10(d). Thus, a 2D flow pattern is found in the closed cavity. With increasing depth, slant reverse flow along the cylinder wall caused strong 3D flow characteristics. For transitional cavity flow, a clear profile with the horse-shoe type is shown in Figs. 10(e)(f).

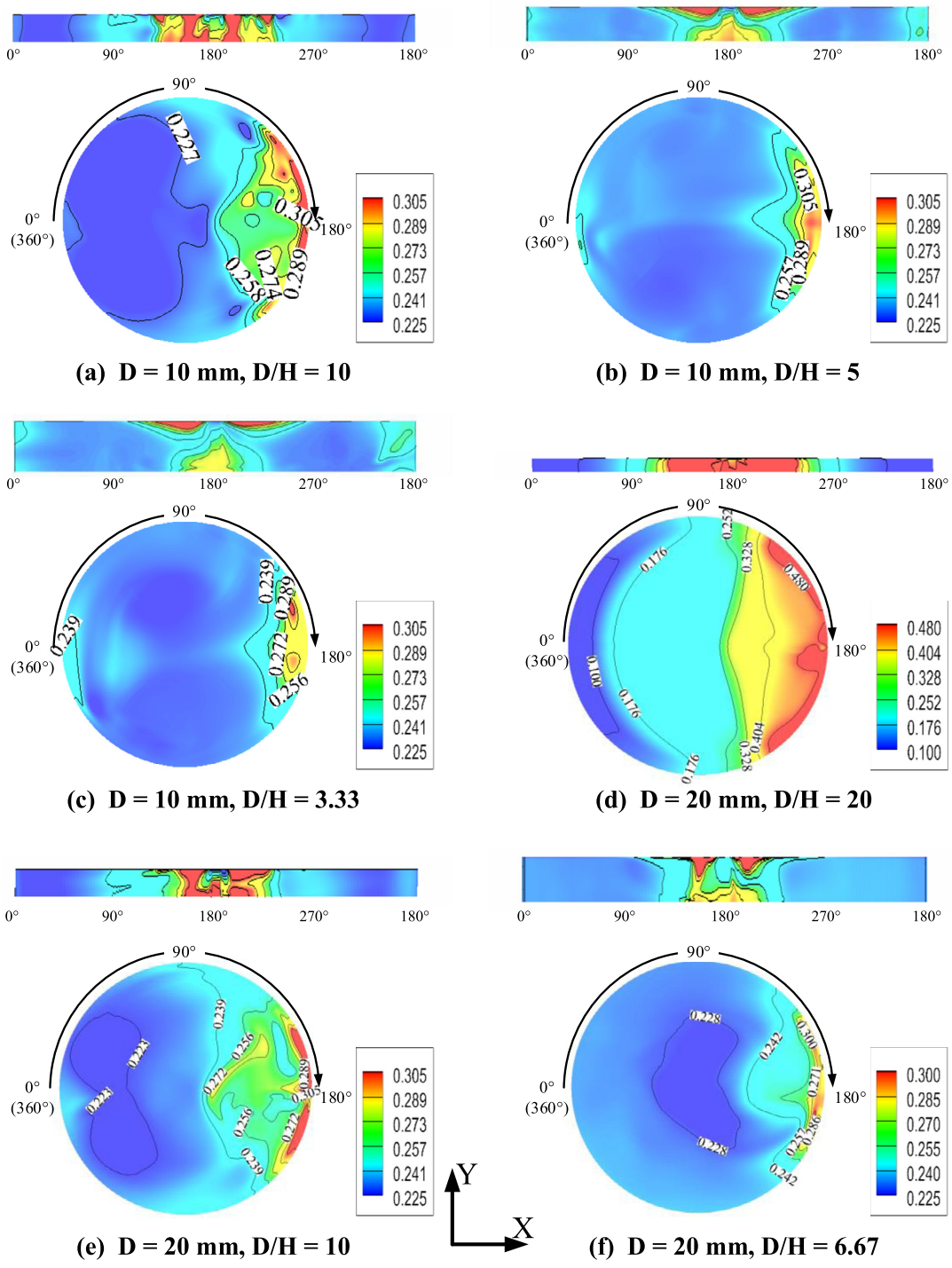

Fig. 10. Distributions and isopleths of Cp of the bottom of cylindrical cavities with different D/H values.

The profile with the beetle-wing type is shown for open cavity flow in Figs. 10(a)–(c). The schematic of Cp distributions is summarized in Fig. 11 for different cavity flow regimes. The Cp distributions along the centerline of cylindrical cavities in the present work coincide with the typical cavity floor distributions for 2D cavity flow at supersonic speeds summarized in reference [3].

4.4. Flow field in the cavity

Fig. 12 shows the streamlines and Mach number distributions of three typical cavity flows at $z/H = -1/2$ and $y/D = 0$ sections. The surface streamlines at the symmetry section of $y/D = 0$ correspond well with the 2D cavity flow. 3D effects of the cylindrical geometry are investigated through the $z/H = -1/2$ section. For open cavity flow ($D/H = 3.33$), two pairs of vortices fulfill the cavity flow and symmetric about the centerline along the flow direction. This finding is due to the free stream bridges over the open cavity. With decreasing cavity depth ($D/H = 10$), new symmetrical vortices develop near the trailing edge of the cavity. In this situation, the free stream is able to turn into the cavity with finite depth and interacts with the cavity end wall. For closed cavity flow ($D/H = 20$), another new pair of symmetrical vortices develop near the leading edges; that is, the free stream can trans-

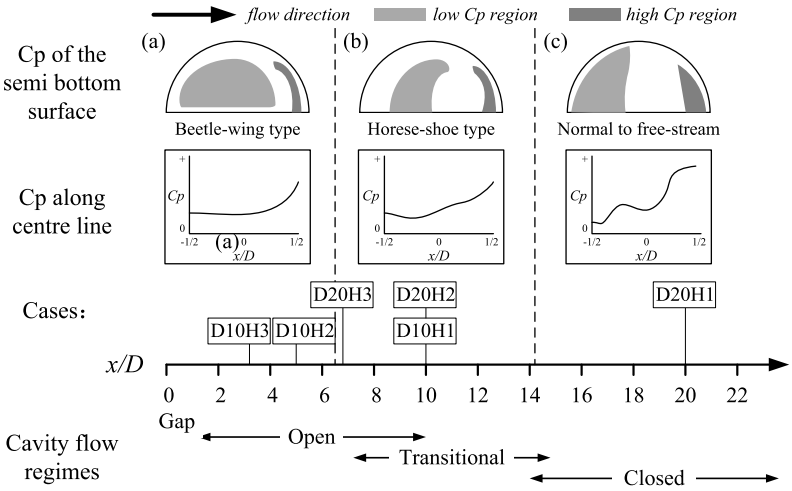

Fig. 11. Schematic of *Cp* including cloud picture for semi bottom surface and distributions along the centerline: (a) open flow, (b) transitional flow, and (c) closed flow. The legends of cloud picture only represent relative value for respective case.

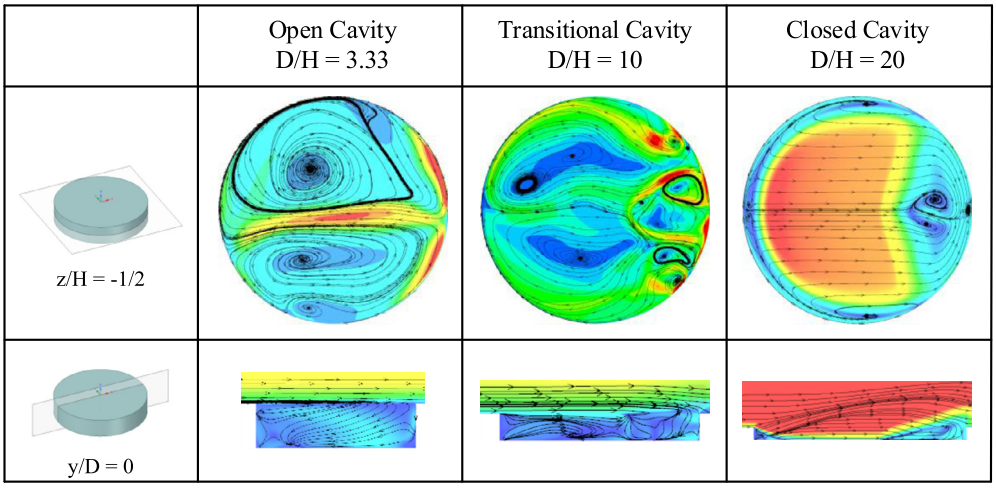

Fig. 12. Streamlines and Mach number distributions of three typical cavity flows at $z/H = -1/2$ and $y/D = 0$ sections.

form into the cavity and impinge on the floor, thereby creating an aft-facing step flow field.

For the transitional and closed cavities in Fig. 12, 3D forward-facing-step vortices are constrained at finite width at both sides of the centerline along the flow direction. Fig. 13(a) shows a schematic of the flow structures induced by a semicylindrical cavity. The chord length of the cylinder along the flow direction is defined as l, as follows:

$$0 \le l \le D$$

The upper and lower bounds of the transitional cavity regime are defined as l_1 and l_2, respectively. The value of l_1 is approximately 10, and the value of l_2 is approximately 14. For the closed cylindrical cavity regime, we have $D/H > l_2$. On the basis of the geometrical features of the cylinder, with the section moving away from the centerline, l decreases gradually, as follows:

$$l_1 \le l \le l_2 \quad \text{for transitional region}$$

$$0 \le l \le l_1 \quad \text{for open flow region}$$

In the open flow region, the free stream is unable to enter the cavity. Therefore, the cavity in this region only has mass interchange. In the transitional region, vortices develop near the trailing edge and further augmenting the heating effects. The forward-facing-step vortices only exist in transitional and closed flow regions. The relative size of open flow and transitional region depends on l_1/H and l_2/H.

As shown in Fig. 13, flow structures are different between a cylindrical cavity and a rectangular cavity. With the increase of the width, the shallow rectangular cavity flow exists significant downwash [27,41] and causing a heat-augment region. Meanwhile, the downstream-side corners of the rectangle would cause strong longitudinal vortices (Fig. 13(b)). Different combinations of D/H and W/H for the rectangular cavity are complex. However, the flow structure caused by geometric characteristics of the rectangular cavity does not exist in the cylindrical cavity. On the one hand, the decrease of the chord length L away from the centerline inhibits the presence of downwash, as discussed above. On the other hand, due to the curved wall of the cylinder, there was no obvious presence of downstream longitudinal vortices.

4.5. Heat flux distributions

Fig. 14 shows the distributions and isopleths of normalized q/q_{ref} heat flux of the bottom of cylindrical cavities with different D/H values. The results of heat flux correspond to the wall pressure distributions in Fig. 14.

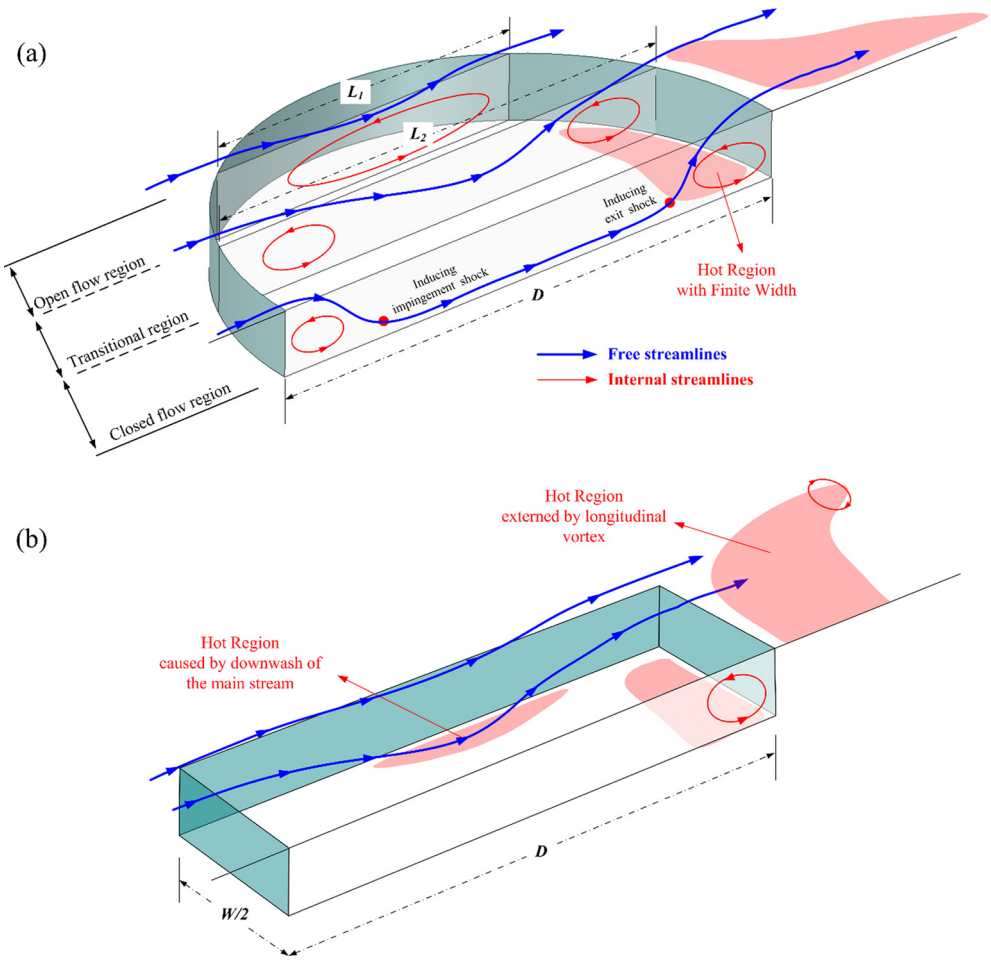

Fig. 13. (a) Schematic of the flow structures induced by a semi-cylindrical cavity, (b) flow structures induced by a semi-rectangular cavity (reproduced for reference [27,41] with additional modification from reference [14]).

For the closed cavity case of $D/H = 20$, as shown in Fig. 14(d), the wall pressure coefficient becomes maximum. The maximum heat transfer coefficient is over five times the value of q_{ref} at the trailing edge of the circular cylindrical surface of the cavity. The heat flux coefficient at the downstream edge of the bottom is approximately 3.05 times the value of q_{ref}. The hot regions are symmetrically distributed about the centerlines (located at approximately 150°/210°). This condition results from the slant recirculating eddy along the cavity circular wall. This comes from the fact that the main part of the flow entering the cavity and blocking the backflow along the centreline. The heat transfer coefficient becomes minimum at the low-pressure area (near the upstream edge of the bottom) with a shape of a slim crescent. The variation of the local heat transfer coefficient is comparatively gradual. This phenomenon corresponds well to the Cp profile (Fig. 10(d)).

With increasing cavity depth, the local value of heat flux remarkably decreases. The hot region expands toward the center of the circle bottom. This comes from the fact that the mainstream does not impinge the bottom directly, as shown in Figs. 14(a)(e), the complex unstable flow structures for the transitional cavity cause the irregular heat-affected zones.

For the open cavity case of $D/H = 3.33$, as shown in Fig. 14(c), the heat flux coefficient at the downstream edge of the bottom is approximately 1.73 times the value of q_{ref}. The maximum heat augment effects are lower than that of closed cavity. Since the mainstream flow bridges the cylindrical cavity and no obvious slant recirculating eddy exists, the width of the hot region for the open cavity is shorter than that of the closed cavity. This phenomenon also corresponds well to the Cp profile (Fig. 10(c)). Flow structure and Cp distribution are the basis for analyzing heat transfer characteristics.

5. Conclusion

In this study, the flow structures and heat transfer characteristics of Mach 5.5 compressible flow over three-dimensional cylindrical cavities are investigated through both experimental and numerical methods. The main conclusions can be summarized as follows:

(1) Generally, the cylindrical cavity flow patterns are symmetrical about the centerline along the flow direction, and slant reverse flow along the cylinder wall causes strong three-dimensional flow characteristics. Moreover, the flow structures of the cylinder cavity depend on not only the ratio of diameter to depth D/H but also the ratio of local chord length to depth l/H. Therefore, for a closed cylindrical cavity flow, symmetrical open flow regions can be also observed at spanwise sides far away from the centerline.

(2) The pressure distributions on the bottom of cylindrical cavities vary with different cavity regimes. For the closed flow, adverse pressure distributions develop near the front wall, and a region of high pressure develops near the aft wall. For the open flow, the pressure profile is relatively flat, and local peaks appear near the aft wall. Moreover, the pressure isoline is approximately parallel and normal to the free stream in the closed flow. And the pressure profiles would take on a beetle-wing

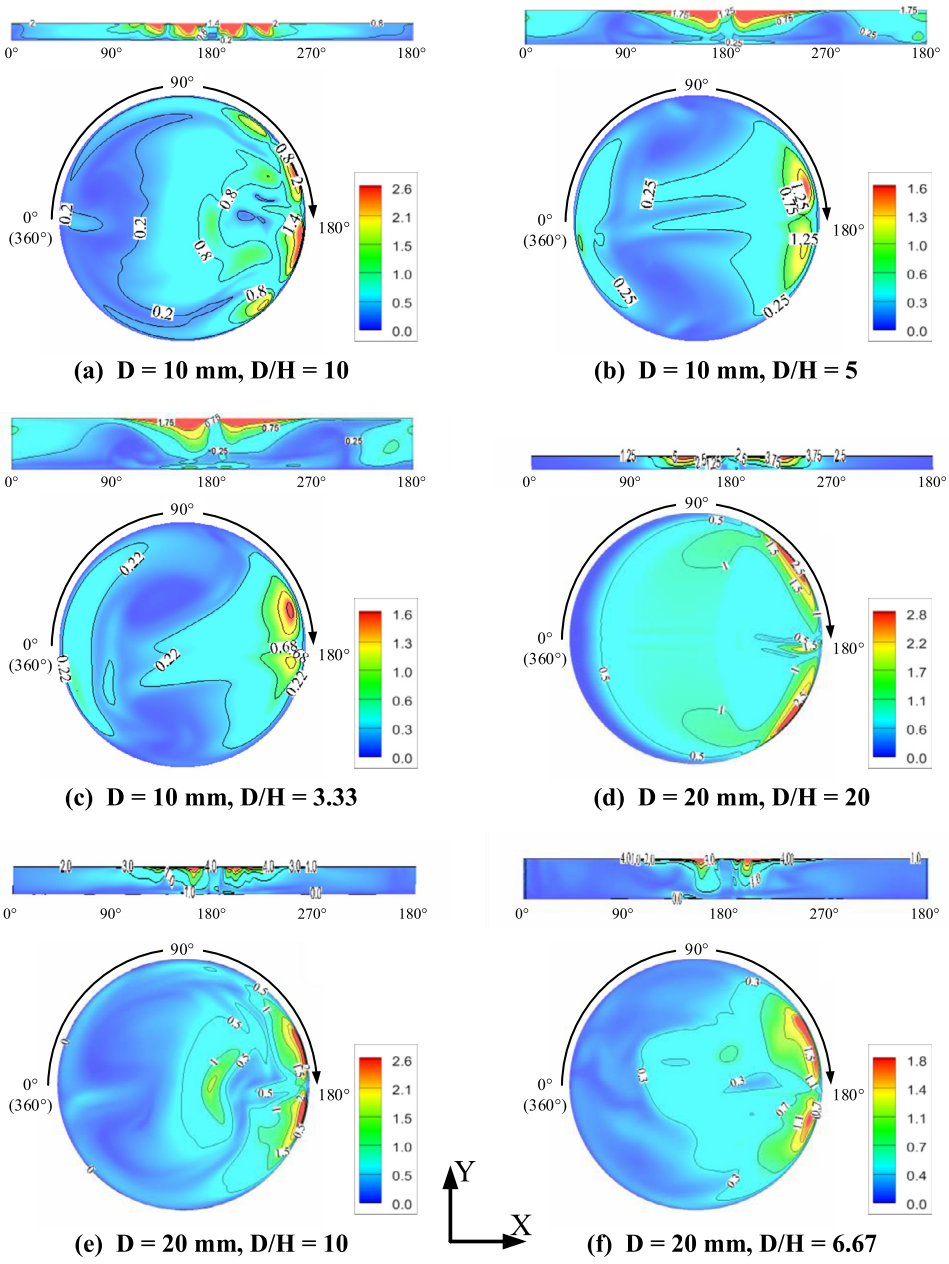

Fig. 14. Distributions and isopleths of q/q_{ref} of the bottom of cylindrical cavities with different D/H values.

shape and a horse-shoe shape in the open and transitional flows, respectively.

(3) High-speed flows over the cylindrical cavity would produce remarkably local heat augments. The heating augmentation is significant near the trailing edge of the cavity and distributed in a finite width along the spanwise direction. Quantitatively, the peak value of cavity induced heat flux is from approximately 1.5 to over 3 times compared with that in flat regions, and the heating augmentation decreases with the decrease in D/H.

To sum up, the details of three-dimensional cylindrical cavity flows are carefully revealed in this paper, which enriches the understanding of the cavity flow regimes under high-speed compressible airflow. In future work, more accurate heat flow measurements should be developed to confirm these initial findings in this study.

Declaration of competing interest

The authors declare that they have no known competing financial interests or personal relationships that could have appeared to influence the work reported in this paper.

Acknowledgement

Financial supports from the National Natural Science Foundation of China (Grant Nos. 11472276 and 11902322) are gratefully acknowledged.

References

[1] E.R. Gowree, C. Jagadeesh, C.J. Atkin, Skin friction drag reduction over staggered three dimensional cavities, Aerosp. Sci. Technol. 84 (2019) 520–529.
[2] K. Karamcheti, Sound Radiation from Surface Cutouts in High Speed Flow, California Institute of Technology, 1956.
[3] S. Lawson, G. Barakos, Review of numerical simulations for high-speed, turbulent cavity flows, Prog. Aerosp. Sci. 47 (2011) 186–216.
[4] K. Taira, M.S. Hemati, S.L. Brunton, Y. Sun, K. Duraisamy, S. Bagheri, S.T. Dawson, C.-A. Yeh, Modal analysis of fluid flows: applications and outlook, AIAA J. 58 (2020) 998–1022.
[5] M.A. Trudgian, W.O. Landsberg, A. Veeraragavan, Experimental investigation of inclining the upstream wall of a scramjet cavity, Aerosp. Sci. Technol. 99 (2020) 105767.
[6] H. Wang, X. Song, L. Li, Y. Huang, M. Sun, Lean blowoff behavior of cavity-stabilized flames in a supersonic combustor, Aerosp. Sci. Technol. 109 (2021) 106427.
[7] H. Wang, Z. Wang, M. Sun, Experimental study of oscillations in a scramjet combustor with cavity flameholders, Exp. Therm. Fluid Sci. 45 (2013) 259–263.
[8] Z. Cai, J. Zhu, M. Sun, Z. Wang, Spark-enhanced ignition and flame stabilization in an ethylene-fueled scramjet combustor with a rear-wall-expansion geometry, Exp. Therm. Fluid Sci. 92 (2018) 306–313.
[9] T. Gao, J. Liang, M. Sun, Symmetric/asymmetric separation transition in a supersonic combustor with single-side expansion, Phys. Fluids 29 (2017) 126102.
[10] C. Liu, J. Yu, Z. Wang, M. Sun, H. Wang, H. Grosshans, Characteristics of hydrogen jet combustion in a high-enthalpy supersonic crossflow, Phys. Fluids 31 (2019) 046105.
[11] M.-B. Sun, X.-D. Cui, H.-B. Wang, V. Bychkov, Flame flashback in a supersonic combustor fueled by ethylene with cavity flameholder, J. Propuls. Power 31 (2015) 976–981.
[12] M. Sun, H. Wang, Z. Cai, J. Zhu, Unsteady Supersonic Combustion, Springer Nature, 2020.
[13] H.W. Gehman, Columbia Accident Investigation Board Report, Columbia Accident Investigation Board, 2003.
[14] J.L. Everhart, Supersonic/hypersonic laminar heating correlations for rectangular and impact-induced open and closed cavities, J. Spacecr. Rockets 46 (2009) 545–560.
[15] R.C. Palharini, W.F. Santos, The impact of the length-to-depth ratio on aerodynamic surface quantities of a rarefied hypersonic cavity flow, Aerosp. Sci. Technol. 88 (2019) 110–125.
[16] A. Charwat, C. Dewey Jr, J. Roos, J. Hitz, An investigation of separated flows-part II: flow in the cavity and heat transfer, J. Aerosp. Sci. 28 (1961) 513–527.
[17] A. Charwat, J. Roos, F. Dewey Jr, J. Hitz, An investigation of separated flows-Part I: the pressure field, J. Aerosp. Sci. 28 (1961) 457–470.
[18] T. Kim, S. Park, S. Lee, D. Yu, H. You, Analysis of flow oscillation due to sidewall of three-dimensional supersonic open cavity flow, Int. J. Aeronaut. Space Sci. 20 (2019) 839–849.
[19] D. Maull, L. East, Three-dimensional flow in cavities, J. Fluid Mech. 16 (1963) 620–632.
[20] C. Shieh, P. Morris, Comparison of two- and three-dimensional turbulent cavity flows, in: 39th Aerospace Sciences Meeting and Exhibit, 2001, p. 511.
[21] E.P. DeMauro, S.J. Beresh, K.M. Casper, J.L. Wagner, J.F. Henfling, R.W. Spillers, Volumetric velocimetry of complex geometry effects on transonic flow over cavities, AIAA J. 57 (2019) 1941–1954.
[22] X. Jin, B. Wang, X. Cheng, Q. Wang, F. Huang, Effects of corner rounding on aerothermodynamic properties in rarefied hypersonic flows over an open cavity, Aerosp. Sci. Technol. 110 (2021) 106498.
[23] C. Zhang, R. Li, Z. Xi, Z. Wan, D. Sun, Effect of Mach number on the mode transition for supersonic cavity flows, Aerosp. Sci. Technol. 106 (2020) 106101.
[24] E. Plentovich, R.L. Stallings, M. Tracy, Experimental cavity pressure measurements at subsonic and transonic speeds, NASA Tech. Pap. 3358 (1993) 1–128.
[25] S.J. Beresh, J.L. Wagner, K.M. Casper, Compressibility effects in the shear layer over a rectangular cavity, J. Fluid Mech. 808 (2016) 116–152.
[26] J.L. Everhart, K.T. Berger, K.S. Bey, N.R. Merski, W.A. Wood, Cavity Heating Experiments Supporting Shuttle Columbia Accident Investigation, 2011.
[27] Y. Ohmichi, K. Suzuki, Flow structures and heating augmentation around finite-width cavity in hypersonic flow, AIAA J. 52 (2014) 1624–1631.
[28] F.R. Verdugo, A. Guitton, R. Camussi, Experimental investigation of a cylindrical cavity in a low Mach number flow, J. Fluids Struct. 28 (2012) 1–19.
[29] V.I. Terekhov, S. Kalinina, Y.M. Mshvidobadze, A review on heat transfer coefficient and aerodynamic resistance on a surface with a single dimple, J. Enhanc. Heat Transf. 24 (2017).
[30] C. Haigermoser, F. Scarano, M. Onorato, Investigation of the flow in a circular cavity using stereo and tomographic particle image velocimetry, Exp. Fluids 46 (2009) 517–526.
[31] K.-M. Chung, K.-H. Lee, K.-C. Chang, Characteristics of cylindrical cavities in a compressible turbulent flow, Aerosp. Sci. Technol. 66 (2017) 160–164.
[32] O. Marsden, C. Bailly, C. Bogey, E. Jondeau, Investigation of flow features and acoustic radiation of a round cavity, J. Sound Vib. 331 (2012) 3521–3543.
[33] M. Hiwada, T. Kawamura, I. Mabuchi, M. Kumada, Some characteristics of flow pattern and heat transfer past a circular cylindrical cavity, Bull. JSME 26 (1983) 1744–1752.
[34] X. Chang, L. Chen, G. Yu, D. Qian, Development of the facility for model scramjet testing, in: 10th AIAA/NAL-NASDA-ISAS International Space Planes and Hypersonic Systems and Technologies Conference, 2001, p. 1857.
[35] S. Zhang, Q. Wang, J. Li, X. Zhang, H. Chen, Coaxial thermocouples for heat transfer measurements in long-duration high enthalpy flows, Sensors 20 (2020) 5254.
[36] D.L. Schultz, T. Jones, Heat-transfer measurements in short-duration hypersonic facilities, in: Advisory Group for Aerospace Research and Development Paris, France, 1973.
[37] J.D. Anderson Jr, Fundamentals of Aerodynamics, Tata McGraw-Hill Education, 2010.
[38] R. Wang, Z. Wang, H. Zheng, H. Song, Comparison of strategies for coupled flow-thermal analysis of thermal protection system at hypersonic flight condition, Int. J. Aeronaut. Space Sci. 21 (2020) 347–362.
[39] H. Zheng, F. Nicolleau, N. Qin, Detached eddy simulation of turbulence flows in a pipe with fractal shape orifices, in: Advances in Turbulence XII, Springer, 2009, pp. 947–948.
[40] H. Zheng, G. Yang, Investigation of aerodynamic performance of high-speed train by detached eddy simulation, in: Proceedings of the 1st International Workshop on High-Speed and Intercity Railways, Springer, 2012, pp. 31–39.
[41] L.H. Xiao, Z.X. Xiao, Z.W. Duan, S. Fu, Improved-delayed-detached-eddy simulation of cavity-induced transition in hypersonic boundary layer, Int. J. Heat Fluid Flow 51 (2015) 138–150.